

Influence of uniform momentum zones on frictional drag within the turbulent boundary layer

Kangjun Wang(王康俊) and Nan Jiang(姜楠)
Citation: Chin. Phys. B, 2021, 30 (**3**): 034703. DOI: 10.1088/1674-1056/abc7a6
Journal homepage: http://cpb.iphy.ac.cn; http://iopscience.iop.org/cpb

What follows is a list of articles you may be interested in

Effect of high-or low-speed fluctuations on the small-scale bursting events in an active control experiment

Xiao-Tong Cui(崔晓通), Nan Jiang(姜楠), and Zhan-Qi Tang(唐湛棋)
Chin. Phys. B, 2021, 30 (**1**): 014702. DOI: 10.1088/1674-1056/abc7a9

Direct numerical simulation on relevance of fluctuating velocities and drag reduction in turbulent channel flow with spanwise space-dependent electromagnetic force

Dai-Wen Jiang(江代文), Hui Zhang(张辉), Bao-Chun Fan(范宝春), An-Hua Wang(王安华)
Chin. Phys. B, 2019, 28 (**5**): 054701. DOI: 10.1088/1674-1056/28/5/054701

Drag reduction characteristics of heated spheres falling into water

Jia-Chuan Li(李佳川), Ying-Jie Wei(魏英杰), Cong Wang(王聪), Wei-Xue Xia(夏维学)
Chin. Phys. B, 2018, 27 (**12**): 124703. DOI: 10.1088/1674-1056/27/12/124703

Coherent structures over riblets in turbulent boundary layer studied by combining time-resolved particle image velocimetry (TRPIV), proper orthogonal decomposition (POD), and finite-time Lyapunov exponent (FTLE)

Shan Li(李山), Nan Jiang(姜楠), Shaoqiong Yang(杨绍琼), Yongxiang Huang(黄永祥), Yanhua Wu(吴彦华)
Chin. Phys. B, 2018, 27 (**10**): 104701. DOI: 10.1088/1674-1056/27/10/104701

Active control of wall-bounded turbulence for drag reduction with piezoelectric oscillators

Jian-Xia Bai(白建侠), Nan Jiang(姜楠), Xiao-Bo Zheng(郑小波), Zhan-Qi Tang(唐湛琪), Kang-Jun Wang(王康俊), Xiao-Tong Cui(崔晓通)
Chin. Phys. B, 2018, 27 (**7**): 074701. DOI: 10.1088/1674-1056/27/7/074701

Influence of uniform momentum zones on frictional drag within the turbulent boundary layer*

Kangjun Wang(王康俊)[1] and Nan Jiang(姜楠)[1,2,†]

[1] Department of Mechanics, School of Mechanical Engineering, Tianjin University, Tianjin 300350, China
[2] Tianjin Key Laboratory of Modern Engineering Mechanics, Tianjin 300072, China

(Received 17 August 2020; revised manuscript received 5 October 2020; accepted manuscript online 5 November 2020)

Based on a set of experimental databases of turbulent boundary layers obtained from particle image velocimetry in the streamwise-wall-normal plane at friction-velocity-based Reynolds number $Re_\tau = 612$, the influence of uniform momentum zones (UMZs) on the skin-friction drag is investigated. The skin-friction drag is measured by the single-pixel ensemble correlation method. The results show that the velocity fields with the number of UMZs larger than the mean value have a relatively low skin-friction drag, while the velocity fields with the number of UMZs less than the mean value have a relatively high skin-friction drag. By analyzing the statistical characteristics of UMZs, the dynamic correlation between the UMZs and skin-friction drag is explored. The velocity fields with a low number of UMZs present a sweep event. These sweep motions intensify the small-scale Reynolds shear stress in the near-wall region by modulation effects. The enhancement of small-scale Reynolds shear stress is the direct reason for the high skin-friction drag. Increasing the proportion of velocity fields with high UMZs amount may be a direction to reduce the skin-friction drag within the TBL.

Keywords: turbulent boundary layers, uniform momentum zones, skin-friction drag

PACS: 47.85.lb, 47.85.ld, 47.27.nb, 47.27.De **DOI:** 10.1088/1674-1056/abc7a6

1. Introduction

Coherent structures in turbulent boundary layers (TBLs) have been the focus of research for five decades. In recent years, the discovery of uniform momentum zones (UMZs) further enhances the community's understanding of the coherent structures within the TBL. UMZ is a large and irregular flow region, in which the fluid has relatively uniform streamwise momentum. The streamwise length of UMZs is approximately 3δ (δ denotes the thickness of the boundary layer), so the UMZs were thought of as a type of large-scale motions (LSMs).[1] In the velocity field obtained from particle image velocimetry (PIV), UMZs can lead the probability density function (PDF) of the streamwise velocity to appear local peaks. Adrian *et al.*[2] defined these local peaks as the modal velocities to characterize approximately identical streamwise velocity of UMZs.

In channel flow, Kwon *et al.*[3] found that the interior of UMZs contains low-level turbulence, while the thin layers demarcating the UMZs have relatively intense vorticity. Eisma *et al.*[4] investigated the internal shear layers in TBL. Their results show that the internal shear layers around UMZs share similar characteristics with the turbulent non-turbulent interface (TNTI), and the growth rate of the LSMs is connected to the entrainment velocity of these internal shear layers. Based on the experimental dataset of four different Re_τ (Re_τ is the friction-velocity-based Reynolds number), de Silva *et al.*[5] detected the number of UMZs within the TBL. They found that the mean number of detected UMZs presents a log-liner law with Re_τ, and the wall-normal thickness of the UMZs furthest away from the wall accounts for the variation of the instantaneous boundary layer height. They further revealed the evidence that the hairpin packets related to the generation of UMZs have hierarchical length-scale distributions within TBL. This discovery coincides with the attached-eddy hypothesis.[6–9] An extension work of Laskari *et al.*[10] showed that the velocity fields with a low number of UMZ are usually linked with a large-scale sweep motion, and in the near-wall region, the small-scale turbulence activity is more intense compared with the fields with high UMZ numbers. This phenomenon is similar to the modulation effect of LSMs to small-scale motion.[11]

Traditionally, the skin-friction drag is thought to be associated with the turbulence activity in the near-wall region, hence the coherent structure in the near-wall region is always the focus of research on skin-friction drag reduction.[12–16] In recent years, the LSMs in the outer regions are also found to have an impact on the generation of skin-friction drag. Hutchins *et al.*[17] observed that a large-scale low skin-friction event within the TBL is associated with the low-speed regions of LSMs. Hwang and Sung[18] found that the high-speed LSMs can amplify the vortical motions in the near-wall region, and then the amplified vortical motions induce the increase of skin friction. The research of skin-friction drag reduction via

*Project supported by the National Natural Science Foundation of China (Grant Nos. 11732010, 11972251, 11872272, 11902218, and 11802195) and the National Key R&D Program of China (Grant No. 2018YFC0705300).

†Corresponding author. E-mail: nanj@tju.edu.cn

© 2021 Chinese Physical Society and IOP Publishing Ltd

flow control in wall-bounded turbulence illustrated that the action of hairpin vortices in the near-wall region is the primary cause of higher skin-friction drag within the TBL compared to the laminar boundary layer.[19–23] As the UMZs belong to the LSMs, the UMZs are also expected to influence the wall shear stress within the TBL.

As to the measurement of skin-friction drag, the measurement method mainly includes the direct and indirect method. The direct methods such as floating element balance, oil-film interferometry, and liquid crystal coatings are inconvenient to use. In addition, these methods are unable to perform measurements under the water. The indirect methods such as Clauser fit and Musker fit need the mean streamwise velocity profile to accord with the standard profile. Compared with the aforementioned methods, the single-pixel ensemble correlation (SPEC) is a newly developed method to acquire the skin-friction drag. The method of SPEC acquires the single-pixel resolution by extending the cross-correlation map of the interrogation window in time dimension. In short, the SPEC method uses temporal resolution to exchange for spatial resolution.[24,25] Own to the high spatial resolution, the SPEC can measure the mean velocity profile in the viscous sublayer, and get a reliable value of skin-friction drag by estimating the slope of the mean streamwise velocity profile in the viscous sublayer.[26,27] The more details of SPEC can be referred to Westerweel *et al.*[24] and Kähler *et al.*[25]

The objective of the present study is to explore the influence of UMZs on the skin-friction drag and to examine the statistic characteristics of UMZs within the TBL. The experimental dataset analyzed in this work was obtained from time-resolved particle image velocimetry (TRPIV). The velocity fields were acquired in the streamwise-wall-normal plane. The method of SPEC was used to measure the skin-friction drag. In Section 2, the experimental facility and measurement method are introduced. In Section 3, the relationships between UMZs and skin-friction drag, and statistic characteristics of UMZs are analyzed. In Section 4, the concluding remarks are given.

2. Experimental setup

The present experiments in TBL were carried out in a low-speed recirculating water channel located at Tianjin University. The test section of the water channel is 6.2 m × 0.29 m ×0.38 m (length × width × height). The turbulent boundary layers were developed on the bottom wall of the test section. A tripwire with a diameter of 2 mm was placed 200 mm downstream of the test section inlet to stimulate the turbulent development. The velocity fields were acquired in the streamwise-wall-normal plane via a 2D TRPIV. The measurements were carried out at the place 2.7 m downstream of the trip. The free-stream turbulence intensity is 1.5% at a typical free-stream velocity $U_\infty = 0.35$ m/s. In present work, x, y, z denotes the streamwise, wall-normal, and spanwise directions, respectively; the corresponding instantaneous velocity and fluctuation velocity components are given by U, V, W and u, v, w; in addition, $\bar{U}, \bar{V}, \bar{W}$ were defined as the mean velocity in the respective direction.

The flow was seeded by polyamide particle with an average diameter of 20 μm and a density of 1.03 g/mm^3. The flow field was illuminated by Litron LDY 304 laser. The thickness of the laser sheet is approximately 2 mm. A Speed Sense 9072 12-bit charge-coupled device (CCD) camera with a 60 mm Nikkor lens was used to record images at a resolution of 800 pixels × 800 pixels. The particle images were acquired with free-stream velocity $U_\infty = 0.359$ m/s, corresponding to $Re_\tau = 612$. Under the aforementioned flow condition, the dataset including 35214 images was acquired with sampling rates $f_s = 750$ Hz. The field of view (FOV) was approximately 1.45δ in x and y directions (57 mm × 57 mm). DynamicStudio software from Dantec was used to transform the particle images to the velocity fields. An adaptive correlation approach was used with interrogation windows of 32 pixels × 32 pixels and an overlap factor of 75%. The spacial distance per vectors was 0.59 mm or 9.23 inner unit. The relative error of the velocity measurements was estimated to be about 1%.

Table 1. Flow parameters of boundary layers.

Free-stream velocity U_∞ (mm/s)	359
Friction velocity u_τ (mm/s)	15.02
Skin friction coefficient C_f	3.502×10^{-3}
Boundary layer thickness δ (mm)	39.2
Displacement thickness δ^* (mm)	6.8
Momentum thickness θ (mm)	4.7
Shape factor H	1.44
Friction velocity Reynolds number Re_τ	612

The CCD camera for SPEC was the same as TRPIV. The fitted lens was a Nikkor lens with a focal length of 200 mm. The corresponding spatial resolution is 0.0207 mm/pixel, which is enough to capture the seeds in the viscous sublayer. As the thickness of the viscous sublayer was very thin, the FOV of the SPEC camera was set as 200 pixels × 50 pixels (4.14 mm × 1.04 mm in the x-direction and y-direction). The cameras for SPEC and TRPIV were synchronized by synchronizer when recording the particle images. The relative error of the skin-friction drag acquired by the SPEC method is related to the number of the ensemble size of image samples. When the ensemble size is above 1000, the relative error is about 1%, while the ensemble size of image samples exceeds 2000, the relative error will be below 0.1%.[27]

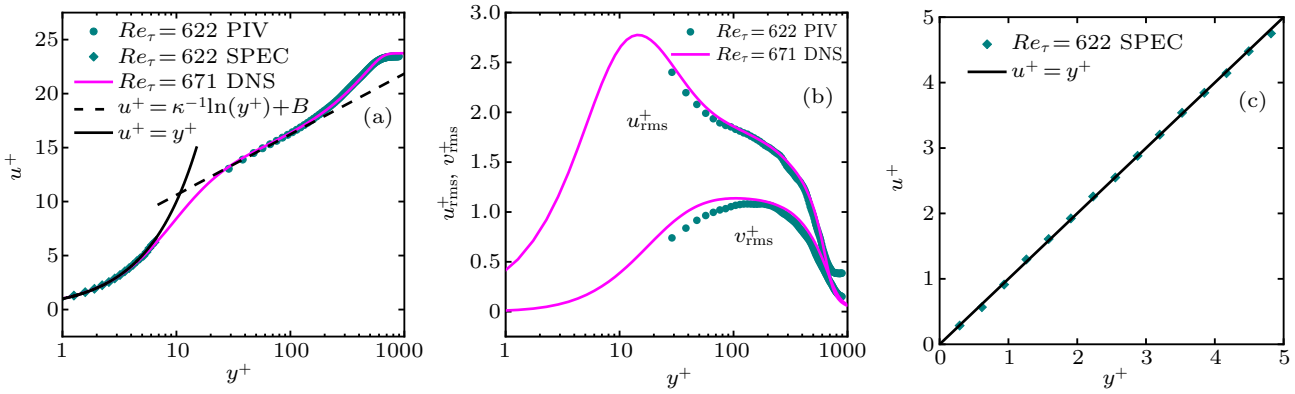


Fig. 1. Profile of (a) mean streamwise velocity and (b) the streamwise and wall-normal turbulent fluctuation intensity. Scatter points represent the experimental result, the magenta line shows the DNS result. The black dashed line and solid line denote the logarithmic region and viscous sublayer. (c) The mean streamwise velocity in the viscous sublayer.

The flow parameters of the boundary layer are listed in Table 1. The log-law constants of mean velocity profile $\kappa = 0.41$ and $B = 5.0$. The friction velocity $u_\tau = 15.02$ mm/s was measured by the SPEC method, and the corresponding goodness of fitting profile slope is greater than 0.9996. Using the Clauser chart method,[28] u_τ was 15.03 mm/s. The u_τ calculated by two different methods almost identical, in the following, we choose $u_\tau = 15.02$ mm/s as the standard value. The boundary layer thickness δ is assessed based on 99% of U_∞. The profiles of mean streamwise velocity and Reynolds normal stress are shown in Figs. 1(a) and 1(b). For comparison, the DNS data of zero-pressure gradient turbulent boundary layer at similar Re_τ by Schlatter and Orlu[29] are posted in the plots in Figs. 1(a) and 1(b), in which the superscript + denotes the nondimensionalization based on inner units. Figure 1(c) exhibits the mean streamwise velocity profile in the viscous sublayer measured by SPEC.

3. Result and discussion

3.1. Influence of uniform momentum zones on frictional drag

In the present study, the methodology proposed by Laskari[10] is used to detect UMZs in the instantaneous velocity fields. This method mainly includes two stages: (1) removing the non-turbulent part of instantaneous velocity fields to exclude the influence of free stream; (2) constructing the PDF based on the turbulent part of instantaneous streamwise velocity. The location of the turbulent/non-turbulent interface (TNTI) in TBL is determined by the method of kinetic energy deficit.[30] In a PIV frame, the local kinetic deficit K is defined as

$$K = 100 \times \frac{1}{9U_\infty^2} \sum_{i,j=-1}^{1} \left[(U_{i,j} - U_\infty)^2 + V_{i,j}^2 \right]. \quad (1)$$

The subscripts i, j denote the relative position to the calculation point in the PIV grid. The fluid in regions with $K < K_{\rm th}$ ($K_{\rm th}$ denotes the threshold) is defined as the non-turbulent part. Thus the $K_{\rm th}$ directly determines the TNTI location. According to the study of Chauhan *et al.*[26] the mean location $\overline{Y}_i$ and the corresponding standard deviation σ_i of the TNTI should satisfy $\overline{Y}_i + 3\sigma_i \approx \delta_{\rm c}$, where the $\delta_{\rm c}$ is the boundary-layer thickness determined from the composite velocity profile of Chauhan *et al.*[31] The iso-contour of instantaneous streamwise velocity in a randomly selected PIV frame is shown in Fig. 2(a). The TNTI is denoted by the blue dashed line in the figure. For PDF construction, the streamwise length of the velocity field is an important factor. In Ref. [32], de Silva *et al.* suggested that the streamwise length in the range of $0.5\delta - 1.2\delta$ can guarantee the UMZs to be identified clearly. In the present study, the streamwise length is set as 1δ, and the corresponding streamwise range in FOV is $[0.2\delta, 1.2\delta]$. As a consequence, the average number of vectors with $U/U_\infty \in [0.4, 1]$ under the TNTI in every PIV frame is approximately 3000. These vectors are distributed in 48 bins of PDF. The size of a bin is approximately $0.5u_\tau$, which is enough for convergence and precision. More detail of the UMZs detection method can be seen in the article of Laskari *et al.*[10] The PDF corresponding to Fig. 2(a) is shown in Fig. 2(b). The location of the PDF local peaks denoted by triangles in the figure represents the modal velocity $U_{\rm m}$ of UMZs.

According to de Silva *et al.*,[5] the UMZs amount $N_{\rm UMZ}$ in a single PIV frame is associated with Re_τ, and the $\bar{N}_{\rm UMZ}$ (the average value of $N_{\rm UMZ}$) shows a log-liner increase with Re_τ increasing. In the present study, $\bar{N}_{\rm UMZ} = 2.79$, this value coincides with the suggestion of de Silva *et al.*[5] In their proposition, the $\bar{N}_{\rm UMZ}$ is approximately 2.75 when $Re_\tau = 600$. Figure 3(a) exhibits the PDF of $N_{\rm UMZ}$. In our dataset, $N_{\rm UMZ}$ belongs to [1, 5], and the corresponding numbers of samples are 1673, 12332, 13998, 6096, and 1112. Based on $N_{\rm UMZ}$, the dataset is classified into 5 groups. In the following, the symbol C_i denoted the group of instantaneous velocity fields with $N_{\rm UMZ} = i$, while the symbol G denoted the ensemble dataset. Figure 3(b) shows the PDF of instantaneous streamwise velocity in different groups. In the figure, we can see that when $U > 0.72U_\infty$ the value of PDF decreases with $N_{\rm UMZ}$, while this trend is reversed when $U < 0.72U_\infty$, and the PDF of G is be-

tween C_2 and C_3. It indicates that the increase of N_{UMZ} can enhance the proportion of low-speed fluid in the fields.

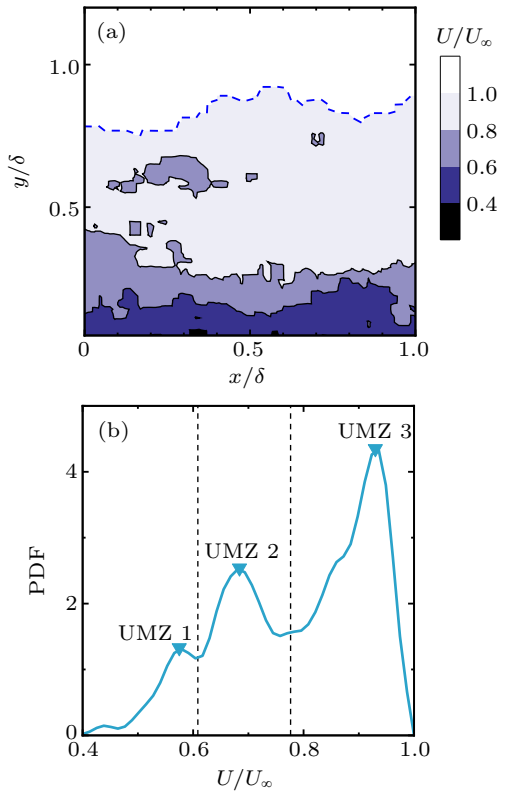


Fig. 2. (a) The iso-contour of U under the TNTI in a randomly selected PIV frame. The TNTI is denoted by the blue dashed line. (b) The PDF corresponding to (a). The location of the peaks denoted by triangles represents the modal velocity U_{m} of UMZs.

Figure 4(a) shows the mean streamwise velocity profile of each group acquired by SPEC in the viscous sublayer. In the figure, the solid lines with color denote the fitted straight line of each profile. The goodness of fit of C_1 to C_5 are 0.9983, 0.9989, 0.9995, 0.9990 and 0.9956. The black dashed line denoted the profile of $u^+ = y^+$, which fits the profile of the ensemble. The slope of the fitted line has a decreasing trend from C_1 to C_5, which indicates that the increase of the N_{UMZ} would reduce the skin-friction drag. The skin-friction coefficient difference $\Delta C_{\mathrm{f},i} = C_{\mathrm{f},i} - C_{\mathrm{f}}$ are exhibited in Fig. 4(b), where the $C_{\mathrm{f},i}$ denote the skin-friction coefficient of C_i. In the figure, the frictional drag of C_1 and C_2 is higher than the ensemble, while C_3, C_4 and C_5 has a lower skin-friction drag compared with the ensemble. The $\Delta C_{\mathrm{f},i} - \Delta C_{\mathrm{f},i+1}$ is also tend to attenuate with N_{UMZ} increasing. In addition, $\bar{N}_{\mathrm{UMZ}} = 2.79$ is close to 3, and the $\Delta C_{\mathrm{f},3}$ is also closest to the zero. It implies that the N_{UMZ} is an important factor to impact the skin-friction drag. Figure 4(c) shows the drag and amount proportion of different groups in the ensemble. The drag proportion of C_1 and C_2 is higher than their amount proportion. While in the group C_3, C_4 and C_5, the drag proportion is lower than the amount proportion. It indicates that increasing the proportion of groups with $N_{\mathrm{UMZ}} > \bar{N}_{\mathrm{UMZ}}$ may be a direction to reduce the skin-friction drag within the TBL.

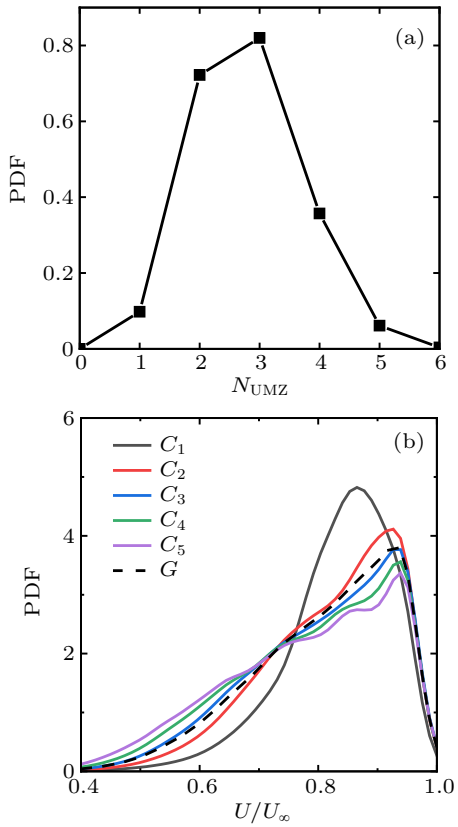


Fig. 3. (a) The PDF of N_{UMZ}. (b) The PDF of instantaneous streamwise velocity in groups C_1 to C_5, and G.

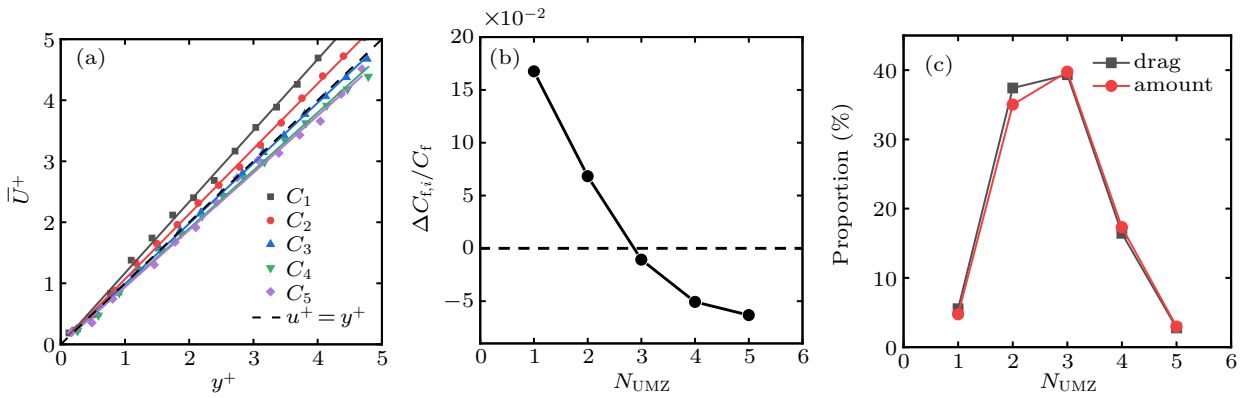


Fig. 4. (a) The mean streamwise velocity profile in each group acquired by SPEC in the viscous sublayer. (b) The difference of skin-friction coefficient between each group and the ensemble. (c) The drag and amount proportion of different groups in the ensemble.

3.2. Statistical characteristics of uniform momentum zones

The spacial location is an important property of UMZs. In the previous literature of de Silva *et al.*[5] and Laskari *et al.*[10] the location of UMZs was defined as the midline of the upper and lower boundary. This definition only reflects the wall-normal distance of UMZs from the wall, so in this paper, the location of UMZs is defined as the centroid of the regions with $U \in [U_m - 0.25u_\tau, U_m + 0.25u_\tau]$ (the $0.5u_\tau$ corresponding to the bin width of PDF construction). The new definition coincides with the criterion that the UMZs are mainly characterized by U_m, and the new definition can reflect the streamwise and wall-normal position information of UMZs in FOV, rather than wall-normal position only. Based on the new definition of location, the UMZs in every single PIV frame are ranked. The symbol R_j presents the jth UMZ form the wall. Because the N_{UMZ} of PIV frames in group C_i is i, so for a certain group, j belongs to [1, j].

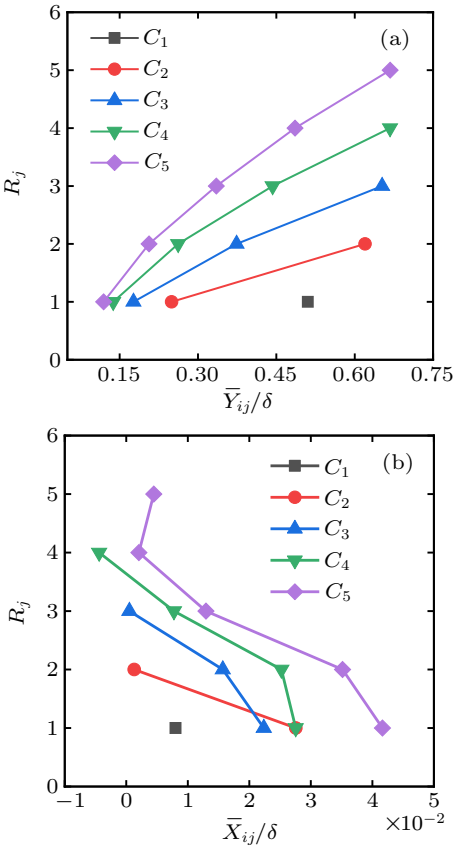


Fig. 5. (a) Mean location of UMZs and (b) modal velocity of UMZs varying with rank R_j and group C_i.

Figure 5 shows the average wall-normal location and stream-wise position of UMZs in FOV. In Fig. 5(a), $\bar{Y}_{ij}$ denotes the average wall-normal location of R_j in C_i. In the figure, we can see $\bar{Y}_{i+1,j} < \bar{Y}_{ij} < \bar{Y}_{i+1,j+1}$. It means that the bottommost UMZs trend to approach the wall with N_{UMZ} increasing, while the topmost UMZs tend to be close to the roof of the TBL. Corresponding to Fig. 5(a), Fig. 5(b) shows the average streamwise position $\bar{X}_{ij}$ of UMZs varying with R_j and C_i, the reference position in streamwise is selected as the center of FOV. In the figure, we can see that $\bar{X}_{ij}$ of UMZs with lower ranks tend to be biased toward the downstream position. Furthermore, for a certain rank the ascent of N_{UMZ} would aggravate this bias. It implies that the centroids of the UMZs with lower wall-normal locations tend to be more downstream compared with the upper UMZs. This is consistent with the inclination of low-momentum zones in the attached eddy model.[8,9]

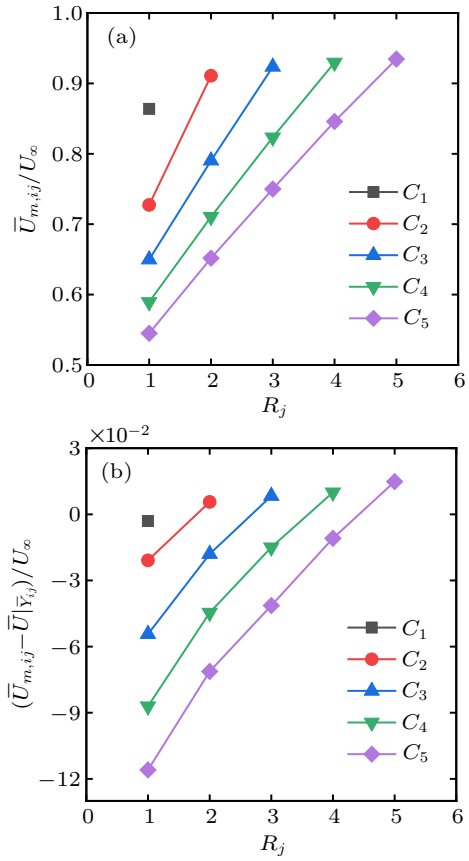


Fig. 6. (a) Mean modal velocity $\bar{U}_{m,ij}$. (b) The difference between the mean modal velocity $\bar{U}_{m,ij}$ and the mean streamwise velocity of global fields at the corresponding wall-normal position $\bar{U}|_{\bar{Y}_{ij}}$.

Figure 6(a) summarizes the mean modal velocity $\bar{U}_{m,ij}$ of UMZs with different R_j and C_i. For a certain rank, the $\bar{U}_{m,ij}$ is descended with N_{UMZ} increasing, and it has $\bar{U}_{m,i+1,j} < \bar{U}_{m,ij} < \bar{U}_{m,i+1,j+1}$. The trend of $\bar{U}_{m,ij}$ varying with R_j and C_i is similar to the $\bar{Y}_{ij}$ in Fig. 5(a). The difference between the $\bar{U}_{m,ij}$ and $\bar{U}|_{\bar{Y}_{ij}}$ (the mean streamwise velocity of ensemble at the wall-normal location $\bar{Y}_{ij}$) are shown in Fig. 6(b). In the figure, apart from the $\bar{U}_{m,22}$, $\bar{U}_{m,33}$, $\bar{U}_{m,44}$ and $\bar{U}_{m,55}$, all the $\bar{U}_{m,ij}$ are less than the corresponding $\bar{U}|_{\bar{Y}_{ij}}$, and for a certain rank the increase of N_{UMZ} would intensify the deficit of velocity. In addition, the $\bar{Y}_{22}$, $\bar{Y}_{33}$, $\bar{Y}_{44}$ and $\bar{Y}_{55}$ are higher than the $\bar{Y}_{11}$ (about 0.51δ), as shown in Fig. 4(a). It is emphasized that the UMZs under the $\bar{Y}_{11}$ are the low momentum zones; the UMZs above the $\bar{Y}_{11}$ are the high momentum zones; the speed of UMZs at $\bar{Y}_{11}$ is close to the global mean. The low momentum zones are

linked to the backward induction of the hairpin vortex packets. Due to the more intense activity of vortices close to the wall, the effect of backward induction can lead to a larger momentum deficit of UMZs at the regions close to the wall.

As discussed above, the UMZs below $\bar{Y}_{11} \approx 0.51\delta$ belongs to the low-speed structures. To further investigate the dynamic correlation between the UMZs and skin-friction drag, the impact of the UMZs on the velocity fields is analyzed. Figure 7 shows the profiles of conditionally averaged streamwise fluctuation velocity $\langle u_i \rangle$ and wall-normal fluctuation velocity $\langle v_i \rangle$:

$$\langle u_i \rangle = \langle u(x,y) | N_{\mathrm{UMZ}} = i \rangle \,, \tag{2}$$

$$\langle v_i \rangle = \langle v(x,y) | N_{\mathrm{UMZ}} = i \rangle \,. \tag{3}$$

In Eqs. (2) and (3), the $\langle \cdot \rangle$ denotes the average over both the samples and the x span. As shown in the plots, $\langle u_i \rangle$ and $\langle v_i \rangle$ of all groups cross the zero line almost at $\bar{Y}_{11} \approx 0.51\delta$. This observation coincides with the result that the convection speed of UMZs in C_1 is close to the ensemble, as shown in Fig. 6(b). Below the $\bar{Y}_{11}$, the velocity fields with $N_{\mathrm{UMZ}} \leq 2$ (C_1, C_2) present a Q4 event ($\langle u_i \rangle > 0$ and $\langle v_i \rangle < 0$), and the intensity of the Q4 event is attenuated with N_{UMZ} increasing. When $N_{\mathrm{UMZ}} \geq 3$ (C_3, C_4, C_5), the velocity fields begin to present a Q2 event ($\langle u_i \rangle < 0$ and $\langle v_i \rangle > 0$), and the intensity of the Q2 event is enhanced with N_{UMZ} increasing. At the location near the $\bar{Y}_{51} \approx 0.12\delta$, a valley appears at the profile of $\langle u_4 \rangle$ and $\langle u_5 \rangle$, meanwhile, a peak appears at the profile of $\langle v_4 \rangle$ in $\langle v_5 \rangle$, as shown in Fig. 7. This observation implies that the UMZs under the $\bar{Y}_{11}$ are a mass of low momentum fluid with an upward motion. It is in line with the conclusion of Adrian *et al.*[2] that the UMZ is generated by the back induction effect of the hairpin packets. The reason why the low momentum UMZs are under the $\bar{Y}_{11}$ is that most of the hairpin packets are populated under the one-half of boundary layer thickness, as proposed by Adrian.[33] Above the $\bar{Y}_{11}$, the variation tendency of profiles is reversed. The velocity fields of C_1 and C_2 present a Q2 event. With N_{UMZ} increasing, the Q2 event is gradually transformed into Q4 event, i.e., the velocity fields of C_3, $C_4$and C_5 present a Q4 event. This can be owned to the high speed of topmost UMZs in C_3, C_4 and C_5. Hence, we can conclude that the high (low) frictional drag in low (high) N_{UMZ} groups ($N_{\mathrm{UMZ}} < 3$ or $N_{\mathrm{UMZ}} > 3$) is attributed to the sweep (eject) motion under the $\bar{Y}_{11}$.

As proposed by Laskari *et al.*,[10] the sweep and ejection in different groups can modulate small-scale turbulent activity. This modulation would change the Reynolds shear stress distribution within the TBL. However, the skin-friction drag is directly related to the Reynolds shear stress in the near-wall region.[34] In order to explore the effect of modulation on the skin-friction drag in different groups, the velocity fields are demarcated as large- and small-scale components using a spectral filter. The cutoff wavelength of the filter in streamwise is set as $\lambda_x = \delta$, which is the same as Hutchins and Marusic.[35] In the following, $\langle u_{\mathrm{Li}} \rangle$ and $\langle u_{\mathrm{Si}} \rangle$ denote the large- and small-scale components of $\langle u_i \rangle$respectively, while $\langle v_{\mathrm{Li}} \rangle$ and $\langle v_{\mathrm{Si}} \rangle$ denote the large- and small-scale components of $\langle v_i \rangle$ respectively.

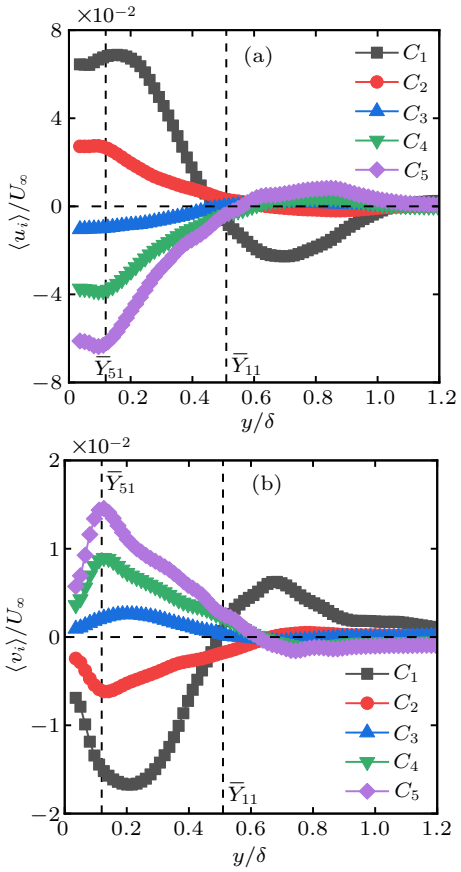


Fig. 7. The profiles of conditionally averaged (a) streamwise fluctuation velocity $\langle u_i \rangle$ and (b) wall-normal fluctuation velocity $\langle v_i \rangle$. The dashed line denotes the location of $\bar{Y}_{51}$ and $\bar{Y}_{11}$.

Figure 8(a) gives the map of conditionally averaged large-scale Reynolds shear stress $-\langle u_{\mathrm{Li}} v_{\mathrm{Li}} \rangle$ and globally averaged large-scale Reynolds shear stress $-\langle u_{\mathrm{L}} v_{\mathrm{L}} \rangle$. Figure 8(b) plots the difference between the conditionally averaged large-scale Reynolds shear stress and globally averaged large-scale Reynolds shear stress, $-\Delta\langle u_{\mathrm{Li}} v_{\mathrm{Li}} \rangle = \langle u_{\mathrm{L}} v_{\mathrm{L}} \rangle - \langle u_{\mathrm{Li}} v_{\mathrm{Li}} \rangle$. When $y < 0.3\delta$, $-\langle u_{\mathrm{L1}} v_{\mathrm{L1}} \rangle$ and $-\langle u_{\mathrm{L5}} v_{\mathrm{L5}} \rangle$ are higher than other groups, while $\langle u_{\mathrm{L3}} v_{\mathrm{L3}} \rangle$ is lowest. It means that the intense sweep in C_1 and ejection in C_5 can enhance large-scale Reynolds shear stress. However, the great valley of the $-\langle u_{\mathrm{L1}} v_{\mathrm{L1}} \rangle$ around the $\bar{Y}_{11}$ reflects that the speed of UMZs in C_1 is very close to the global mean, as shown in Fig. 6(b). Figure 8(c) exhibits the conditionally averaged small-scale Reynolds shear stress $-\langle u_{\mathrm{Si}} v_{\mathrm{Si}} \rangle$ and globally averaged small-scale Reynolds shear stress $-\langle u_{\mathrm{S}} v_{\mathrm{S}} \rangle$, while Fig. 8(d) shows their difference $-\Delta\langle u_{\mathrm{Si}} v_{\mathrm{Si}} \rangle = \langle u_{\mathrm{S}} v_{\mathrm{S}} \rangle - \langle u_{\mathrm{Si}} v_{\mathrm{Si}} \rangle$. Similar to the profiles of $\langle u_i \rangle$ and $\langle v_i \rangle$, the profiles of $-\Delta\langle u_{\mathrm{Si}} v_{\mathrm{Si}} \rangle$ are also cross the zero line around the one point, but the crossover point is around the $\bar{Y}_{51} \approx 0.12\delta$ (which is denoted by the black dashed line in Fig. 8(d)). Below the $\bar{Y}_{51}$, the value of

$-\Delta\langle u_{\rm Si}v_{\rm Si}\rangle$ decreases with $N_{\rm UMZ}$. This trend is consistent with the skin frictional drag varying with $N_{\rm UMZ}$. It indicates that the sweep in $C_{i<3}$ enhances the skin-friction drag by intensifying the small-scale Reynolds shear stress in the near-wall region.

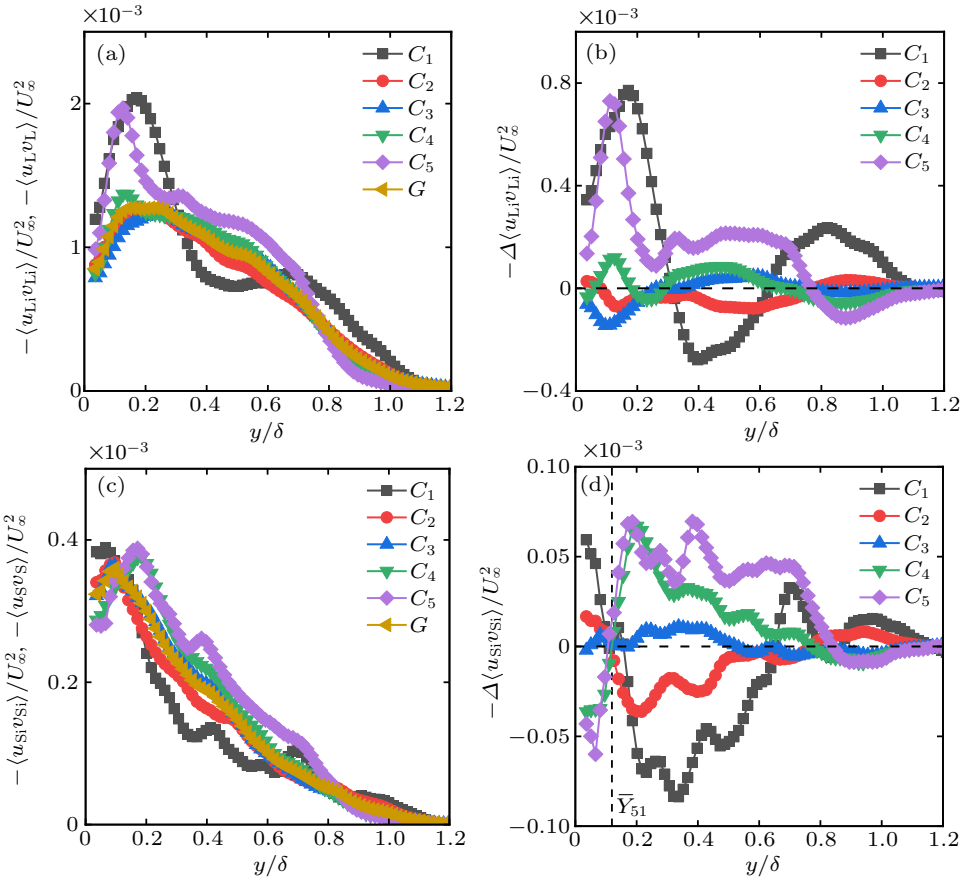


Fig. 8. (a) Conditionally averaged large-scale Reynolds shear stress $-\langle u_{\rm Li}v_{\rm Li}\rangle$ and globally averaged large-scale Reynolds shear stress $-\langle u_{\rm L}v_{\rm L}\rangle$. (b) The difference between the $-\langle u_{\rm Li}v_{\rm Li}\rangle$ and $-\langle u_{\rm L}v_{\rm L}\rangle$, $-\Delta\langle u_{\rm Li}v_{\rm Li}\rangle = \langle u_{\rm L}v_{\rm L}\rangle - \langle u_{\rm Li}v_{\rm Li}\rangle$. (c) Conditionally averaged small-scale Reynolds shear stress $-\langle u_{\rm Si}v_{\rm Si}\rangle$ and globally averaged small-scale Reynolds shear stress $-\langle u_{\rm S}v_{\rm S}\rangle$. (d) The difference between the $-\langle u_{\rm Si}v_{\rm Si}\rangle$ and $-\langle u_{\rm S}v_{\rm S}\rangle$, $-\Delta\langle u_{\rm Si}v_{\rm Si}\rangle = \langle u_{\rm S}v_{\rm S}\rangle - \langle u_{\rm Si}v_{\rm Si}\rangle$.

4. Conclusion

A dataset of velocity fields is acquired in the streamwise-wall-normal plane within the TBL, by a 2D TRPIV. The method of SPEC is used to measure the skin-friction drag of TBL. The influence of UMZs on the skin-friction drag and statistical characteristics of UMZs is investigated. The results show that the skin-friction drag is linked with the number of UMZs in velocity fields. When the number of UMZs is larger than the mean value, the velocity fields have a relatively low skin-friction drag. When the number of UMZs is less than the mean value, the velocity fields have a relatively high skin-friction drag. By defining the centroid of the regions with $U \in [U_{\rm m}-0.25u_\tau, U_{\rm m}+0.25u_\tau]$ as the location of UMZs, the information on the spatial distribution of the UMZs is exhibited. In spatial distribution, the UMZs with lower wall-normal locations tend to be more downstream compared with the upper UMZs. The UMZs under the 0.51δ are the low momentum zones, the UMZs above the 0.51δ are the high momentum zones. At 0.51δ, the speed of UMZs is close to the global mean. The conditionally averaged fluctuation velocity shows that, below the 0.51δ, the velocity fields with the low number of UMZs present a Q4 event, and with $N_{\rm UMZ}$ increasing, the Q4 event is gradually transformed into a Q2 event. The velocity fields with a low number of UMZs intensify the small-scale Reynolds shear stress in the near-wall region to enhance the skin-friction drag by modulation effect. Increasing the proportion of velocity fields with high UMZs amount may be a direction to reduce the skin-friction drag within the TBL.

References

[1] Meinhart C D and Adrian R J 1995 *Phys. Fluids* **7** 694
[2] Adrian R J, Meinhart C D and Tomkins C D 2000 *J. Fluid Mech.* **422** 1
[3] Kwon Y S, Philip J, De Silva C M, Hutchins N and Monty J P 2014 *J. Fluid Mech.* **751** 228
[4] Eisma J, Westerweel J, Ooms G and Elsinga G E 2015 *Phys. Fluids* **27** 055103
[5] De Silva C M, Hutchins N and Marusic I 2016 *J. Fluid Mech.* **786** 309
[6] Townsend A A 1980 *The Structure of Turbulent Shear Flow* 2nd edn (Cambridge: Cambridge University Press)
[7] Perry A E and Chong M S 1982 *J. Fluid Mech.* **119** 173
[8] Marusic I and Perry A E 1995 *J. Fluid Mech.* **298** 389
[9] Perry A E and Marusic I 1995 *J. Fluid Mech.* **298** 361
[10] Laskari A, R de Kat, R J Hearst and B Ganapathisubramani 2018 *J. Fluid Mech.* **842** 554
[11] Baars W J, K M Talluru, N Hutchins and I Marusic 2015 *Exps. Fluids* **56** 10

[12] Lang S S, Geng X G and Zang D Y 2014 *Acta Phys. Sin.* **63** 084704 (in Chinese)
[13] Mei D J, Fan BC, Chen Y H and Ye J F 2010 *Acta Phys. Sin.* **59** 8335 (in Chinese)
[14] Han Y, Zhang H, Fan B C, Li J, Jiang D W and Zhao Z J 2017 *Chin. Phys. B* **26** 084704
[15] Li S, Jiang N, Yang S Q, Huang Y X and Wu Y H 2018 *Chin. Phys. B* **27** 104701
[16] Li S, Jiang N and Yang S Q 2019 *Acta Phys. Sin.* **68** 074702 (in Chinese)
[17] Hutchins N, Monty J P, Ganapathisubramani B, Ng H C H and Marusic I 2011 *J. Fluid Mech.* **673** 255
[18] Hwang J and Sung H J 2017 *J. Fluid Mech.* **829** 751
[19] Bai H L, Y Zhou, W G Zhang, S J Xu, Y Wang and R A Antonia 2014 *J. Fluid Mech.* **750** 316
[20] Tian H P, Zhang J X, Jiang N and Yao Z H 2015 *Exp. Therm. Fluid Sci* **69** 27
[21] Zheng X B, Jiang N and Zhang H 2016 *Chin. Phys. B* **25** 014703
[22] Bai J X, Jiang N, Zheng X B, Tang Z Q, Wang K J and Cui X T 2018 *Chin. Phys. B* **27** 074701
[23] Jiang D W, Zhang H, Fan B H and Wang A H 2019 *Chin. Phys. B* **28** 054701
[24] Westerweel J, Geelhoed P F and Lindken R 2004 *Exps. Fluids* **37** 375
[25] Kähler C J, Scholz U and Ortmanns J 2006 *Exp. Fluids* **41** 327
[26] Wang J, Pan C and Wang J 2020 *Phys. Rev. Fluids* **5** 074605
[27] Shen J, Pan C and Wang J 2014 *Sci. Chin.-Phys. Mech. Astron.* **57** 1352
[28] Clauser F H 1954 *J. Aero. Sci* **21** 91
[29] Schlatter P and R Örlü 2010 *J. Fluid Mech.* **659** 116
[30] Chauhan K, Philip J, De Silva C M, Hutchins N and Marusic I 2014 *J. Fluid Mech.* **742** 119
[31] Chauhan K A, Monkewitz P A and Nagib H M 2009 *Fluid Dyn. Res.* **41** 021404
[32] De Silva C M, Hutchins N and Marusic I 2014 *19th Australasian Fluid Mechanics Conference*, December 8–11, 2014, Melbourne, Australia
[33] Adrian R J 2007 *Phys. Fluids* **19** 041301
[34] Fukagata K, Iwamoto K and Kasagi N 2002 *Phys. Fluids* **14** 13
[35] Hutchins N and Marusic I 2007 *Phil. Trans. R. Soc. Lond. A* **365** 647